ACS APPLIED MATERIALS & INTERFACES

Letter

www.acsami.org

Pure Platinum Nanostructures Grown by Electron Beam Induced Deposition

Chris Elbadawi, Milos Toth, and Charlene J. Lobo*

School of Physics and Advanced Materials, University of Technology, Sydney, P.O. Box 123, Broadway, New South Wales 2007, Australia

ABSTRACT: Platinum has numerous applications in catalysis, nanoelectronics, and sensing devices. Here we report a method for localized, mask-free deposition of high-purity platinum that employs a combination of room-temperature, direct-write electron beam induced deposition (EBID) using the precursor $Pt(PF_3)_4$, and low temperature (≲400 °C) postgrowth annealing in H_2O. The annealing treatment removes phosphorus contaminants through a thermally activated pathway involving dissociation of H_2O and the subsequent formation of volatile phosphorus oxides and hydrides that desorb during annealing. The resulting Pt is indistinguishable from pure Pt films by wavelength dispersive X-ray spectroscopy (WDS).

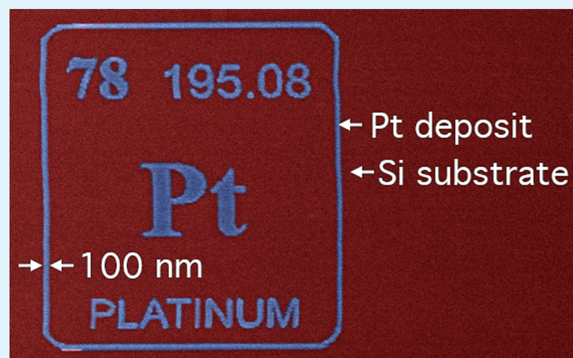

KEYWORDS: *electron beam induced deposition, nanofabrication, nanostructured platinum, catalysis, direct-write, maskless lithography*

INTRODUCTION

Vapor-phase fabrication of nanoscale metals most commonly employs organometallic precursors. Gas-mediated, focused electron beam induced deposition (EBID)[1] is one such fabrication technique that offers several advantages over commonly employed technologies like chemical vapor deposition and atomic layer epitaxy. Most significantly, EBID permits room-temperature localized deposition with high (<10 nm) resolution without the use of lithographic masks and resists.[2,3] Structures fabricated using EBID include nanodot (Figure 1a) and wire arrays,[2−4] magnetic nanowires,[5] and tips for magnetic force microscopy,[6] contacts to nanowires and carbon nanotubes,[7] plasmonic nanostructures[8] and metallic seeds used to catalyze the growth of individual nanowires.[9] The main limitation of EBID is that the deposited materials are typically highly impure, consisting of metal or oxide grains with a diameter of ∼1−5 nm embedded in an amorphous matrix rich in precursor ligand constituents.[1,6,10−18] The precursors are often organometallics and the matrix generally contains ≳50 at % carbon, yielding deposits that behave as granular materials with percolative transport properties.[11−14,19]

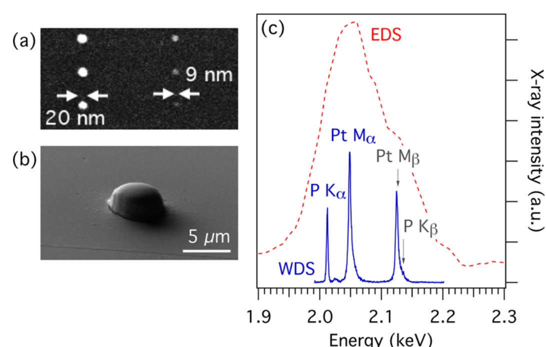

Figure 1. SEM images of a (a) nanodot array grown by $Pt(PF_3)_4$-mediated EBID using a Gaussian electron beam, and (b) deposit grown using a 5 μm, top-hat beam. (c) X-ray spectra showing the Pt K_α, Pt M_α, Pt M_β, P K_α, and K_β X-ray lines.

Previously, relatively high-purity EBID-grown materials have been realized in a limited number of cases, where (i) low-carbon-content precursors are available,[20−26] (ii) substrate heating or precursor gas mixtures are used to improve purity,[26−32] (iii) ultrahigh-vacuum techniques are used to produce ultraclean, reactive substrate surfaces,[33,34] or (iv) annealing, ozone, electron or plasma processing is used to modify as-grown deposits.[1,8,10,35,36] However, EBID purity is inadequate for the fabrication of most devices and functional materials (one notable exception is EBID of Co using $Co_2(CO)_8$ as the growth precursor, where a Co content in excess of 90%[37,38] has been realized).

Fabrication of Pt has attracted more attention than any other EBID-grown material. However, to date, there exists no technique for EBID of highly pure Pt. Best results have so far been achieved using the precursor $Pt(PF_3)_4$,[21−26,35] which yields deposits in which phosphorus and fluorine are the major contaminants (oxygen is missing from most prior analyses). We note that high purity Pt deposits have been demonstrated using a combination of an EBID-grown seed layer and atomic layer deposition (ALD),[39] or by XeF_2-mediated, fluorine-induced

Received: August 1, 2013
Accepted: September 19, 2013
Published: September 20, 2013

ACS Publications © 2013 American Chemical Society

decomposition of $Pt(PF_3)_4$ adsorbates.[40] However, both of these techniques exhibit lateral growth rates that are approximately equal to the corresponding vertical growth rates. They can therefore not be used for the growth of high resolution, high aspect ratio deposits, and limit the attainable geometries of self-supporting three-dimensional nanostructures.

Here, we demonstrate the fabrication of highly pure platinum achieved by EBID of $Pt(PF_3)_4$ in combination with postgrowth removal of phosphorus contaminants by low temperature annealing in H_2O. The deposits contain >94 at. %Pt, and are indistinguishable from reference Pt standards by wavelength dispersive X-ray spectroscopy (WDS). The required annealing temperature is sufficiently low (≤400 °C) to prevent both the decomposition of the Pt deposits and chemical etching of the substrate (which are observed at higher annealing temperatures). The purification method is both more effective and more widely applicable than prior methods involving substrate heating during EBID, and postdeposition annealing in vacuum, O_2 and NH_3 environments.

■ METHODS AND MATERIALS

The EBID precursor tetrakis(trifluorophosphine) platinum $Pt(PF_3)_4$ (Strem chemicals) is a high vapor pressure liquid at room temperature. It was loaded into a peltier-cooled stainless steel crucible under dry N_2, which was subsequently removed using multiple freeze−pump−thaw cycles. EBID was performed using an environmental scanning electron microscope (SEM) equipped with a thermionic tungsten hairpin electron source. An in situ environmental subchamber enabled control over the substrate temperature during EBID, as described in references 29 and 41. The subchamber was isolated from a differentially pumped electron column using a 200 μm pressure limiting aperture. After pump-down to $\sim 1 \times 10^{-4}$ Pa, the pressure in the subchamber was maintained at 13 Pa using a pressure-feedback gas delivery system. A 10 keV, 10 nA, top-hat electron beam[17,18] was defocused to a diameter of ∼5 μm, yielding an electron beam flux of $\sim 3 \times 10^{17}$ $e^-/cm^2/s$. Deposits such as the one shown in Figure 1(b) were grown using a stationary, normal incidence beam on Si (111) substrates (with a native oxide), with a growth time of 30 min.

After deposition, samples were transferred in air to an ex-situ vacuum chamber (base pressure $\sim 10^{-4}$ Pa) equipped with a heating stage and a gas flow delivery system. Annealing was performed in vacuum, and in H_2O, O_2 and NH_3 environments (pressure ∼130 Pa). Compositional analysis was performed using a high vacuum SEM equipped with WDS. WDS was used instead of the more common energy dispersive X-ray spectroscopy (EDS) because WDS enables resolution of the P K_α and Pt M_α X-ray peaks which overlap in EDS spectra, as shown in Figure 1c. WDS was performed using a beam energy of 10 keV to ensure that the electron interaction volume (simulated using standard Monte Carlo simulators of electron-solid interactions[42] was contained within the deposit (such as the one shown in Figure 1b). Standards of known elemental composition were used to quantify WDS data, with a reproducibility of ±2%. Each deposit was analyzed once only, either after growth, or after a single postgrowth anneal.

■ RESULTS AND DISCUSSION

As-Grown Deposits. Deposits grown at room temperature have a typical atomic composition of 47 ± 5% Pt, 30 ± 5% P and 15 ± 10% O. The composition variation is greater than the WDS analysis error of ±2% because of variations between individual deposits. The spread is caused by variations in electron beam current typical of thermionic tungsten hairpin electron sources (the deposit composition is known to vary with the beam current density used for $Pt(PF_3)_4$ EBID),[22] and because of uncontrolled partial decomposition of $Pt(PF_3)_4$ by residual gas molecules present in the vacuum chamber. The measured F content decreased with time when samples were stored in vacuum or in air, and was at or below the WDS detection limit in samples stored overnight prior to WDS analysis. The most likely F removal pathway involves the desorption of chemisorbed fluorine, which is expected to be accelerated by H_2O adsorbates[40] with an overall reaction of the form:

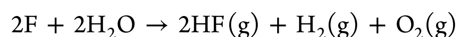

$$2F + 2H_2O \rightarrow 2HF(g) + H_2(g) + O_2(g)$$

The trace amounts of fluorine and the presence of oxygen in the as-grown deposits indicate efficient dissociation and desorption of PF_3 and fluorine during EBID, accompanied by oxidation of phosphorus by residual contaminants (mainly H_2O) present in the vacuum chamber. These results correspond well with those of prior ultrahigh vacuum surface science studies which show that the deposition process involves these reaction pathways[25,26]

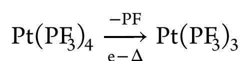

$$Pt(PF_3)_4 \xrightarrow[e-\Delta]{-PF} Pt(PF_3)_3$$

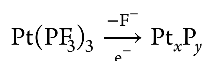

$$Pt(PF_3)_3 \xrightarrow[e^-]{-F^-} Pt_xP_y$$

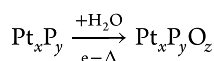

$$Pt_xP_y \xrightarrow[e-\Delta]{+H_2O} Pt_xP_yO_z$$

The last two pathways, involving P−F bond cleavage, and phosphorus oxidation by residual water vapor, occur concurrently under prolonged e-beam irradiation (e^-) and/or substrate heating (Δ) during deposition. Substrate heating during deposition can significantly improve the composition of some EBID-grown materials.[10,27−29] However, in the present case of $Pt(PF_3)_4$-EBID, the deposit composition was observed to improve only at temperatures ≳100 °C, reaching a Pt content of ∼72 at % at ∼120 °C. This extent of purification is inadequate, and the approach is impractical because $Pt(PF_3)_4$ has a thermal decomposition temperature of ∼130 °C.[43] Thermal decomposition of the adsorbates causes delocalized (chemical vapor) deposition, thereby compromising the localized, direct-write capability of EBID.

Postgrowth Annealing. Figure 2 shows the composition of deposits annealed in vacuum ($P \approx 1 \times 10^{-4}$ Pa) for one hour at temperatures of 400, 600, and 750 °C. Temperatures ≳600 °C caused significant structural decomposition of the deposits, illustrated by the image shown in Figure 2. Annealing in vacuum at temperatures ≤600 °C caused an insignificant decrease in the concentration of phosphorus impurities in the deposits. Similarly, annealing in O_2 and NH_3 environments had no significant effect on composition at temperatures lower than the deposit decomposition temperature.

Conversely, low temperature annealing in H_2O vapor can increase the Pt content to a degree that is indistinguishable from reference, high purity Pt films by WDS analysis. Figure 3 shows the deposit composition as a function of H_2O annealing time at 250 and 400 °C. At 400 °C, annealing times of 20, 40, and 300 min yield Pt concentrations of ∼75, 92, and 94 at %, and P concentrations of ∼17, 2, and 2 at %, respectively (where

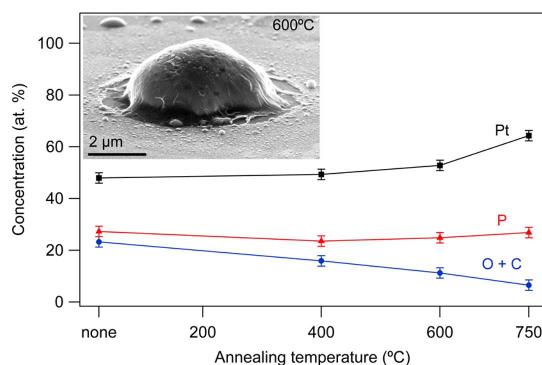

Figure 2. Deposit composition as a function of postgrowth annealing temperature in vacuum (annealing time = 60 min). Inset: SEM image of a deposit acquired after a 600 °C annealing treatment.

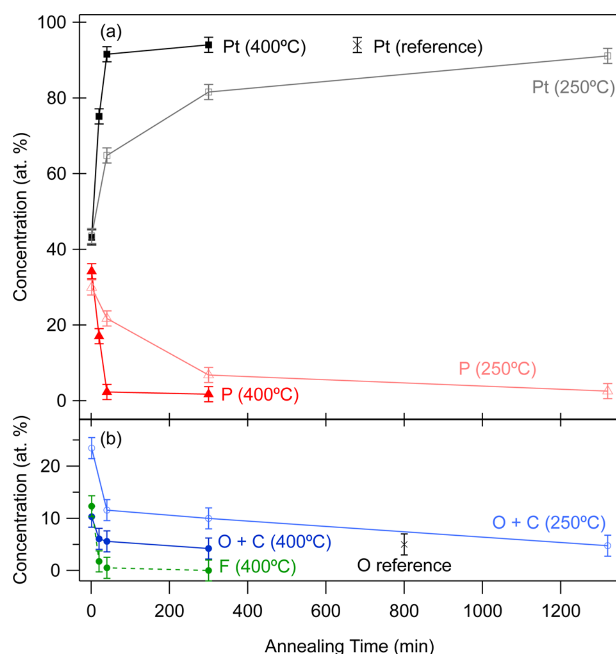

Figure 3. Composition of $Pt(PF_3)_4$-EBID deposits plotted as a function of annealing time in H_2O vapor at 250 and 400 °C. Fluorine was detected only in the sample set annealed at 400 °C, because it was stored in vacuum prior to WDS analysis. The measured composition of a reference, high purity Pt film is also shown in the figure (×).

2 at % is the P detection limit). The Pt concentration of ∼94 at % is indistinguishable from that of a high purity, reference Pt film. The remaining ∼5 at % (Figure 3b) consists of oxygen and carbon, likely because of an oxide layer and oxygen-containing hydrocarbon contaminants that build up on the deposit surface[44] during WDS analysis.

Postgrowth annealing at 400 °C did not cause structural decomposition of the deposits (see, for example, the image in Figure 1b, which shows a deposit that had been annealed in H_2O for 60 min). We note, however, that some degree of shrinkage is expected as a result of purification.[35,36]

Annealing in H_2O at 250 °C yields the same trend as at 400 °C, but significantly longer times (approaching 24 h) are needed to achieve equivalent Pt content (Figure 3). At 600 °C, annealing times of <40 min are needed to produce deposits which are indistinguishable from reference Pt films. However, the high temperature annealing treatment causes thermal decomposition of the deposits (as in high vacuum, see Figure 2), and etching of the substrates in the vicinity of annealed deposits (shown in Figure 4). Etching at high temperatures is

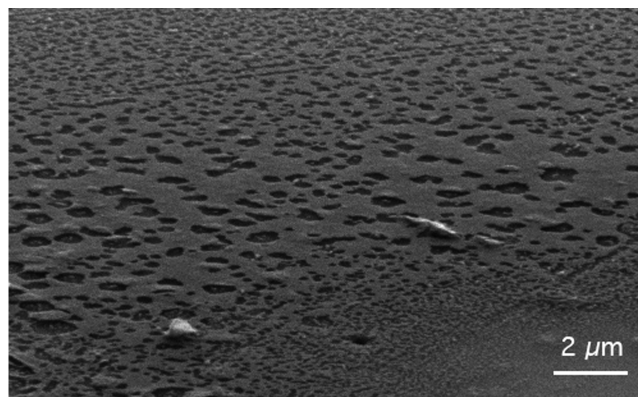

Figure 4. Etch pits in the substrate surface near deposits subjected to a 600 °C anneal in H_2O.

ascribed to phosphoric acid (H_3PO_4) formed in a reaction with residual H_2O molecules present in the vacuum chamber, and is consistent with the reported[45] dependency of the etch rates of silicon and silicon dioxide on temperature.

We note that, of the sample sets shown in Figure 3, F was detected only in the one annealed at 400 °C because it was stored in vacuum prior to WDS analysis (the F concentration decreased with time, as noted above). However, fluorine contamination is not of concern because the H_2O annealing treatment is very efficient at removing F, as seen in Figure 3b.

Purification Mechanism and Generality of the Purification Technique. Our annealing results indicate that removal of phosphorus by the H_2O annealing treatment is likely caused by: (i) thermal decomposition of H_2O at the sample surface into reactive species such as O, H, and OH radicals, and (ii) reaction of P with these radicals to form volatile species that desorb from the solid during annealing. The volatile reaction products likely include P_4O_6, PH_3, and other phosphorus hydrides and oxides, some of which may decompose further as a result of additional reactions with H_2O.

The rate limiting step of the purification process is ascribed to diffusion through the bulk of either the reactive species or the reaction products. WDS can not be used to differentiate between these two mechanisms. It can, however, be used to show that P is removed from the deposit bulk by performing WDS as a function of electron beam energy. Figure 5 shows such data obtained using energies of 10, 15, and 20 keV, from a deposit that was ∼600 nm tall. The spectra show that at 20 keV, the electron beam penetrates the deposit, generating Si X-rays from the substrate but not generating any P K_α signal above the WDS detection limit.[46] The absence of P shows that the H_2O annealing treatment can be used to purify bulk deposits. The underlying mechanism implies that the purification time will scale with deposit size and geometry. Diffusion most likely occurs throughout the amorphous, phosphorus-containing matrix, and along Pt grain boundaries (the deposits are known to be comprised of pure Pt nanocrystallites embedded in an impure, amorphous matrix[24]).

The observed decay in F content with time at room temperature suggests that most of the fluorine is present in the form of residual fragments produced by partial decomposition of $Pt(PF_3)_4$. We note that the fluorine affects WDS analysis, and is responsible for variations in the measured O content of

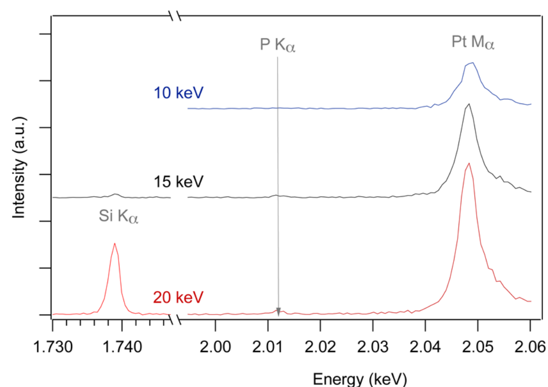

Figure 5. X-ray spectra obtained using electron beam energies of 10, 15, and 20 keV of a $Pt(PF_3)_4$-EBID deposit that had been purified using a 40 min, 400 °C anneal in H_2O (deposit height ~600 nm).

as-grown deposits such as that seen in Figure 3b. Specifically, the greater the time between EBID growth and WDS analysis, the lower the measured F content and the greater the measured O and P content.

The WDS quantification method assumes a uniform distribution of the elemental constituents throughout the electron interaction volume. However, the detected F (as well as O and C impurities that build up during WDS) are most likely concentrated at the deposit surface, and the content of these impurities is therefore overestimated by WDS analysis. Despite these limitations, our H_2O annealing results show that the resulting Pt deposits are indistinguishable from reference Pt films, independent of the initial deposit composition. Specifically, variations in composition caused by deposition parameters such as the beam current density, the moisture content of the vacuum chamber used for EBID, and postgrowth air exposure time do not affect the efficacy of the purification method. This is significant because, to date, the highest purity EBID-grown Pt deposits have been realized using $Pt(PF_3)_4$, which is water vapor sensitive and yields a deposit composition that varies with beam current density.[22]

CONCLUSION

We have demonstrated a method enabling localized, mask-free deposition of pure platinum that employs a combination of room temperature, direct-write electron beam induced deposition (EBID) using the inorganic precursor $Pt(PF_3)_4$, and low-temperature (≤400 °C) postgrowth annealing in H_2O. The annealing treatment removes phosphorus contaminants through a thermally activated pathway involving fragmentation of H_2O adsorbates to produce O and H species that react with P to form volatile phosphorus hydrides and oxides.

AUTHOR INFORMATION

Corresponding Author

*E-mail: Charlene.Lobo@uts.edu.au.

Notes

The authors declare no competing financial interest.

REFERENCES

(1) Utke, I.; Moshkalev, S.; Russell, P. *Nanofabrication Using Focused Ion and Electron Beams: Principles and Applications*; Oxford University Press, New York, 2012.
(2) Van Dorp, W. F.; Van Someren, B.; Hagen, C. W.; Kruit, P. *Nano Lett.* **2005**, *5*, 1303−1307.
(3) Toth, M.; Lobo, C. J.; Knowles, W. R.; Phillips, M. R.; Postek, M. T.; Vladár, A. E. *Nano Lett.* **2007**, *7*, 525−530.
(4) Rykaczewski, K.; Hildreth, O. J.; Kulkarni, D.; Henry, M. R.; Kim, S.-K.; Wong, C. P.; Tsukruk, V. V.; Fedorov, A. G. *ACS Appl. Mater. Interfaces* **2010**, *2*, 969−973.
(5) Fernández-Pacheco, A.; Serrano-Ramón, L.; Michalik, J. M.; Ibarra, M. R.; De Teresa, J. M.; O'Brien, L.; Petit, D.; Lee, J.; Cowburn, R. P. *Sci. Rep.* **2013**, *3*, 1492.
(6) Utke, I.; Hoffmann, P.; Berger, R.; Scandella, L. *Appl. Phys. Lett.* **2002**, *80*, 4792−4794.
(7) Gopal, V.; Radmilovic, V. R.; Daraio, C.; Jin, S.; Yang, P. D.; Stach, E. A. *Nano Lett.* **2004**, *4*, 2059−2063.
(8) Hoeflich, K.; Yang, R. B.; Berger, A.; Leuchs, G.; Christiansen, S. *Adv. Mater.* **2011**, *23*, 2657−2661.
(9) Jenke, M. G.; Lerose, D.; Niederberger, C.; Michler, J.; Christiansen, S.; Utke, I. *Nano Lett.* **2011**, *11*, 4213−4217.
(10) Botman, A.; Mulders, J. J. L.; Hagen, C. W. *Nanotechnology* **2009**, *20*, 372001.
(11) Rotkina, L.; Lin, J.-F.; Bird, J. P. *Appl. Phys. Lett.* **2003**, *83*, 4426−4428.
(12) Rotkina, L.; Oh, S.; Eckstein, J. N.; Rotkin, S. V. *Phys. Rev. B* **2005**, *72*, 233407.
(13) Porrati, F.; Sachser, R.; Schwalb, C. H.; Frangakis, A. S.; Huth, M. *J. Appl. Phys.* **2011**, *109*, 063715.
(14) Porrati, F.; Kämpken, B.; Terfort, A.; Huth, M. *J. Appl. Phys.* **2013**, *113*, 053707.
(15) Utke, I.; Michler, J.; Gasser, P.; Santschi, C.; Laub, D.; Cantoni, M.; Buffat, P. A.; Jiao, C.; Hoffmann, P. *Adv. Eng. Mater.* **2005**, *7*, 323−331.
(16) Bernau, L.; Gabureac, M.; Erni, R.; Utke, I. *Angew. Chem., Int. Ed.* **2010**, *49*, 8880−8884.
(17) Li, J.; Toth, M.; Tileli, V.; Dunn, K. A.; Lobo, C. J.; Thiel, B. L. *Appl. Phys. Lett.* **2008**, *93*, 023130.
(18) Li, J. T.; Toth, M.; Dunn, K. A.; Thiel, B. L. *J. Appl. Phys.* **2010**, *107*, 103540.
(19) Sachser, R.; Porrati, F.; Schwalb, C.; Huth, M. *Phys. Rev. Lett.* **2011**, *107*, 206803:1−5.
(20) Utke, I.; Hoffmann, P.; Dwir, B.; Leifer, K.; Kapon, E.; Doppelt, P. *J. Vac. Sci. Technol., B: Microelectron. Nanometer Struct.* **2000**, *18*, 3168−3171.
(21) Wang, S.; Sun, Y.-M.; Wang, Q.; White, J. M. *J. Vac. Sci. Technol., B: Microelectron. Nanometer Struct.* **2004**, *22*, 1803−1806.
(22) Barry, J. D.; Ervin, M.; Molstad, J.; Wickenden, A.; Brintlinger, T.; Hoffman, P.; Meingailis, J. *J. Vac. Sci. Technol., B: Microelectron. Nanometer Struct.* **2006**, *24*, 3165−3168.
(23) Botman, A.; Hesselberth, M.; Mulders, J. J. L. *J. Vac. Sci. Technol., B: Microelectron. Nanometer Struct.* **2008**, *26*, 2464−2467.
(24) Botman, A.; Hagen, C. W.; Li, J.; Thiel, B. L.; Dunn, K. A.; Mulders, J. J. L.; Randolph, S.; Toth, M. *J. Vac. Sci. Technol., B: Microelectron. Nanometer Struct.* **2009**, *27*, 2759−2763.
(25) Landheer, K.; Rosenberg, S. G.; Bernau, L.; Swiderek, P.; Utke, I.; Hagen, C. W.; Fairbrother, D. H. *J. Phys. Chem. C* **2011**, *115*, 17452−17463.
(26) Rosenberg, S. G.; Landheer, K.; Hagen, C. W.; Fairbrother, D. H. *J. Vac. Sci. Technol., B: Microelectron. Nanometer Struct.* **2012**, *30*, 051805.
(27) Córdoba, R.; Sesé, J.; Teresa, J. M. D.; Ibarra, M. R. *Microelectron. Eng.* **2010**, *87*, 1550−1553.
(28) Mulders, J. J. L.; Belova, L. M.; Riazanova, A. *Nanotechnology* **2011**, *22*, 055302.
(29) Bishop, J.; Lobo, C.; Martin, A.; Ford, M.; Phillips, M.; Toth, M. *Phys. Rev. Lett.* **2012**, *109*, 146103.
(30) Molhave, K.; Madsen, D. N.; Rasmussen, A. M.; Carlsson, A.; Appel, C. C.; Brorson, M.; Jacobsen, C. J. H.; Boggild, P. *Nano Lett.* **2003**, *3*, 1499−1503.
(31) Folch, A.; Tejada, J.; Peters, C. H.; Wrighton, M. S. *Appl. Phys. Lett.* **1995**, *66*, 2080−2082.
(32) Perentes, A.; Hoffmann, P. *Chem. Vap. Deposition* **2007**, *13*, 176−184.

(33) Lukasczyk, T.; Schirmer, M.; Steinruck, H. P.; Marbach, H. *Small* **2008**, *4*, 841−846.
(34) Lukasczyk, T.; Schirmer, M.; Steinruck, H. P.; Marbach, H. *Langmuir* **2009**, *25*, 11930−11939.
(35) Ervin, M. H.; Chang, D.; Nichols, B.; Wickenden, A.; Barry, J.; Melngailis, J. *J. Vac. Sci. Technol., B: Microelectron. Nanometer Struct.* **2007**, *25*, 2250−2254.
(36) Riazanova, A. V.; Rikers, Y. G. M.; Mulders, J. J. L.; Belova, L. M. *Langmuir* **2012**, *28*, 6185−6191.
(37) Fernández-Pacheco, A.; De Teresa, J. M.; Córdoba, R.; Ibarra, M. R. *J. Phys. D: Appl. Phys.* **2009**, *42*, 055005.
(38) Serrano-Ramón, L.; Cordoba, R.; Alfredo Rodriguez, L.; Magen, C.; Snoeck, E.; Gatel, C.; Serrano, I.; Ricardo Ibarra, M.; Maria De Teresa, J. *ACS Nano* **2011**, *5*, 7781−7787.
(39) Mackus, A. J. M.; Mulders, J. J. L.; van de Sanden, M. C. M.; Kessels, W. M. M. *J. Appl. Phys.* **2010**, *107*, 116102.
(40) Randolph, S.; Botman, A.; Toth, M. *Particle* **2013**, *30*, 672−677.
(41) Lobo, C. J.; Martin, A.; Phillips, M. R.; Toth, M. *Nanotechnology* **2012**, *23*, 375302.
(42) Hovington, P.; Drouin, D.; Gauvin, R. *Scanning* **1997**, *19*, 1−14.
(43) Friedman, J. F.; Miller, T. M.; Friedman-Schaffer, J. K.; Viggiano, A. A.; Rekha, G. K.; Stevens, A. E. *J. Chem. Phys.* **2008**, *128*, 104303.
(44) Hern, J.; Goldstein, G. I.; Joy, D. C. *Introduction to Analytical Electron Microscopy*; Plenum Press, 1st ed., 1979.
(45) Van Gelder, W.; Hauser, V. E. *J. Electrochem. Soc.* **1967**, *114*, 869−872.
(46) Monte Carlo simulations[42] were used to verify that the detected P, Pt, and Si X-rays are not strongly self-absorbed by the samples.